

# **A year in the life of the Shackleton space domain awareness station**

**Jeffrey E. Van Cleve, David P. Osterman, Anna Lawitzke, Jacob D. Griesbach,  
Christopher J. Grant, Colleen Olson, and James Contreras**  
*Ball Aerospace, Colorado*

## **ABSTRACT**

A proposed Shackleton Space Domain Awareness (SDA) Station is composed of two solar-powered lunar surface observatories for SDA [1, 2]. At a minimum, each observatory has a wide field-of-view (WFOV) camera for finding objects within 6000 km of the lunar surface and a fisheye camera for finding brighter objects within 200 km of the surface, which are moving too rapidly to be reliably captured by the more sensitive WFOV camera. An enhanced sensor suite might also include thermal, dust, and gas sensors to monitor surfaces in permanently shadowed regions and detect rocket plume and excavation activity. The two sites have complementary solar illumination on their 2.0 m solar power masts, so that at least one of them is operating 95% of the time. The first site, on the Shackleton-de Gerlache Connecting Ridge, has been identified as an attractive base location for South Pole resource exploration and extraction [10]. The complementary site is on the rim of Shackleton Crater [9] and will be able to see what is going on inside the crater as well as in the skies above it. Our method is to identify promising areas from the literature, then do an initial site assessment with using Lunar Reconnaissance Orbiter (LRO) digital elevation maps (DEMs) and the horizon elevation method [3]. We then calculate solar illumination and communication timelines and outage duration histograms using DEMs imported into STK. The illumination model then sets the requirements on power storage and thermal control for night survival. This story plays out over a year, with topographic rising and setting of the Earth, Sun, the Lunar Gateway, and LunaNet comm relays. We discuss the tradeoff between polar field of regard (FOR) and direct LOS communication to Earth, if such a capability is desired before high-bandwidth lunar comm relays are available. As a built flight hardware example, we discuss operations planning for the Ball-built L-CIRiS camera hosted on NASA's Haworth Crater science mission as a lunar polar surface operations planning example.

## **1 Introduction: Exploration of Cislunar Mission Space**

### **1.1 Overview of the Cislunar Domain**

While SDA has historically been practiced in the LEO to GEO domains, the growing quantity of missions and traffic to cislunar space drives the importance and need for above-GEO (XGEO) SDA. As an example, NASA's ARTEMIS and CLPS programs, AFRL's CHPS, and the future planned Chinese activities will lead to numerous assets and rocket bodies launched into the Earth-Moon gravitational corridor in the coming years. Cislunar SDA systems will be critical to protecting and maintaining operational confidence for safe transit.

XGEO distances are generally an order-of-magnitude beyond those typically implemented for GEO sensing, driving the need for high-performance, long-range optical systems. The same sensors that may be adequate for proliferated LEO satellite systems will be insufficient to monitor the vastness of XGEO space. Even cislunar space traffic management (STM) requires a higher sensitivity optical system than SDA in GEO due to the long ranges, larger search volumes, and complex cislunar orbits. Observability in the cislunar corridor is also challenging and limited due to lunar, earth, and solar angular exclusion zones. Because of this, one or more lunar surface-based observers are required to completely cover the  $4\pi$  steradian cislunar regime by tracking low lunar orbit satellites and incoming lunar landers.

### **1.2 Why Look Up From the Moon?**

In the context of the broad cislunar space discussed above, we propose observing stations looking upward from the surface of the Moon for several reasons. First, the lunar surface and near-Moon space is a boundary of cislunar space. Cislunar SDA then includes tracking objects as they enter or leave low orbits around the moon, or land and take off from the lunar surface, to account for objects throughout their life cycle. Second, the lunar surface and near-Moon space are very difficult to observe from , or even from sensors in geosynchronous or Earth-Moon Lagrange point stations, because of lunar straylight, surface clutter for transiting targets, and invisibility of occulted targets. Third, we expect various parties to have high-value assets on the lunar surface itself, which with judicious site selection might be observable from the sites selected for the SDA mission. Companion papers at this conference discuss

complementary approaches to observing this region: a joint SDA-LUNINT (lunar surface intelligence) mission [4] which combines limited awareness of the surface with Lagrange-zone SDA in a single sensor, and awareness of the surface as seen from above [5] which complements the awareness of space as seen from the surface discussed in this paper.

A South Pole station is of particular importance because it will soon be the focus of exploration activity, attracted by resources of water ice and persistent solar illumination in the permanently-shadowed regions (PSRs) and on high points on crater rims, respectively. While such proximities of ice and light also exist in the north polar region, the preponderance of evidence shows the south polar region is much richer in resources than the north polar region [6]. A Shackleton station – centrally located in the polar region at the pole itself -- can watch comings and goings in the skies above all of the resource-rich South Pole region [1]. A site of this station perched on the crater rim can peer into the crater itself or dispatch rovers on short (100 m) traverses to look over the edge.

The value of SDA from Moon-based sensors is discussed in [7, 8], who present a method for optimizing lunar sensor placements to observe objects in certain families of Lagrange orbits.

### 1.3 Lunar Surface Observatory Findings

Last year we [1] made these findings about lunar surface observatories (LSOs):

- “Go Solar and Polar” – the 4x cost difference between nuclear and solar power station more than compensates for the reduced duty cycle of solar vs. nuclear power, especially at the poles where favorable lighting conditions increase the solar duty cycle. Thus, we are studying detailed solar illumination at S. Pole in this paper.
- A Wide Field of View (FOV) camera (WFOV) which looks for objects out to ~6000 km from the lunar surface covers the zone hidden from Earth-based and Lagrange Point observers by lunar straylight. We will not be revisiting WFOV in this paper.
- A fisheye camera is needed to see bright, nearby, high angular rate targets. These targets fly overhead so quickly the WFOV may be looking the other way doing a sky scan while they pass overhead, while the fisheye camera stares unblinking at the zenith. The optical design of the fisheye camera is developed in §3.1.

## 2 Sun and Shadow – Topographical Analysis for Site Selection and Operations

### 2.1 History of the Illuminati Part 1

Modeling the illumination of the lunar surface and solar power masts on landers and rovers is essential for site selection, night survival engineering, and operations planning for non-nuclear missions on the lunar surface. One approach is to directly use images from LRO’s Lunar Reconnaissance Orbiter Camera (LROC) to identify persistently illuminated regions [9]. These images have GSDs between 0.5 and 2.0 m and good temporal coverage at the poles. A complementary approach is to model illumination conditions in the lunar polar regions using the LRO laser altimeter DEMs and their derivatives (slope models) and compare them to LROC images, as in [3] and developed in more depth in [10, 12]. We will apply the local horizon method [3] to calculate Sun and Earth visibility from a mast on the lunar surface near the South Pole. While [3] also present a singly-scattered illumination model for the permanently-shadowed regions (PSRs), we will use the analytical spherical bowl-shaped crater model introduced in [11] and developed in a companion paper [5] to estimate the visible and thermal emissions in PSRs, such as the interior of Shackleton Crater. The complementary problem, of modeling the Moon as seen from above, is treated by [12] and discussed in more detail in our companion paper [5].

Reference [9] also discusses meter-scale masts, 100 m-scale mobility, and multi-site operations to improve the solar operability of polar surface stations, up to 95% for a collection of 3 sites on high points the rim of Shackleton Crater. We apply those ideas here and show detailed timelines and outage duration histograms for an interesting site pair.

### 2.2 Communication Scenarios

In the long term, it is hard to imagine a significant amount of activity at the lunar South Pole – especially involving human beings – without a robust lunar communications network as envisioned by NASA’s LunaNet. China has already started to build such a lunar comm network, with the operational *Queqiao* relay satellite providing comm coverage of Farside to support Chang’e 4 and a new lunar relay satellite to support the South polar landing of Chang’e 6 planned for 2024 [14]. In addition, at the time of this writing it was announced [13] that Blue Canyon Technologies is building two Farside comm satellites to support a Farside CLPS (Commercial Lander Payload Services) mission in

2025, possibly with some polar access depending on the orbit design. Thus, it is not unreasonable to make the approximation that comm is almost always available, and each site's operability is governed only by solar illumination. However, it may be desirable to establish an initial operating capability (IOC) before LunaNet is built out, using either the Lunar Gateway or direct-with-Earth (DWE) comm. Whitley & Martinez [15] found that the S. Polar region has 86% communication coverage from the Gateway's Near-Rectilinear Halo (NRHO) orbit, corresponding to a one-day outage in the 7-day period orbit. We apply this result to the Zimovan-Spreen [16] 9:2 synodic resonance orbit, which avoids eclipses and has a period of 6.56 days and hence a 22 h comm outage.

DWE comm can be approximated as half the month on, half the month off, since the elevation of the Earth as seen from the Polar regions varies between -6 and +6 degrees during a month, which is large compared to the lunar obliquity to the Ecliptic (1.5 degrees). Hence, DWE derives much less benefit from topography than solar illumination, and on the rim of Shackleton DWE will be unavailable ~40% of the month, for a 12-day comm outage. This is not attractive due to data volume and latency problems. However, it may be worth considering DWE for IOC for a location on the Nearside near 85S, which is in some sense a compromise between Earth and Sun outages (§2.7). This strategy has been adopted by the NASA mission carrying the Ball-built L-CIRiS camera to Haworth Crater (4W, 86.9S), which we discuss in detail in the next Section.

### 2.3 Lunar Surface Operations Planning

Several common issues are likely to arise in operational planning for many lunar surface instruments, including a number that have been addressed in the development of Ball's L-CIRiS (Lunar Compact Infrared Radiometer in Space) instrument. A primary example consists of operational constraints imposed by the variations in the lunar surface thermal environment, the latter a result of several time-dependent factors: sun direction and angle, surface-reflected illumination, lander shadowing and, for rover operations, rover location and orientation. Operational planning must take account of instrument temperature changes, impact of sun position on radiator efficiency and other effects that may restrict the timing and frequency of science tasks. In some cases, this might include ceasing operations during the thermal environment extremes, or confining certain tasks, to specific parts of the lunar day. Other factors impacting lunar surface planning include the cadence of communication to the Earth, timing of data transfer from instruments to the lander, and availability of instrument telemetry in real or recorded time. Contingency planning may be critical to account for some indeterminacy in landing conditions. Examples include the actual lander orientation with respect to the Sun, reflected light and thermal radiation conditions, and impact of plume scouring beneath and in proximity to the lander.

### 2.4 Horizon Elevation from DEMs

We implemented the horizon elevation method [3] in MATLAB, with the exception that we use the native stereographic projection polar DEMs from the MIT Imbrium server instead of reprojecting to gnomonic, which introduces errors which are small sufficiently close to the Pole. We used the 80 deg S, 40 m pixel polar map LDEM\_80S\_40M.IMG because higher resolution at the same latitude limit gives MATLAB memory errors while limiting the latitude to 85 S or 87.5 S can lead to the calculated horizon being off the map. Nor have we implemented horizon maps for scale or efficiency since we are just spot-checking promising sites from the literature rather than doing an exhaustive search for persistently-illuminated locations across the map; we just calculate the angular horizon elevation for each promising site from the literature. We use JPL-HORIZONS ephemerides for sub-solar longitude and latitude. The sub-solar longitude and latitude are then converted to Elevation and Azimuth for any desired point on the lunar surface using the standard equatorial to horizontal coordinate transformation, in which hour angle is the angle between the site and the sub-solar longitude. These transformations obviate the need to calculate a HORIZONS ephemeris for each site on the lunar surface to get Elevation and Azimuth. The reference ephemeris is the 13 months following 3/7/2025, though the Station sites could operate for several years if Chang'e 4 is a good example.

If the elevation of the middle of the solar disk is less than elevation of landscape at the azimuth of the sun, then we consider the site to be unavailable at that time. We don't integrate over a partial solar disk as in [3]. We group these times into outages to calculate the distribution of outage durations. The same method is used for the Sun and the Earth, without nuance about the location of the ground station for DWE communication.

### 2.5 Site 1: Shackleton-de Gerlache Connecting Ridge C1

Reference [10] used LRO DEMs to compile a list of locations at the lunar poles with high average illumination at surface level averaged over a twenty-year period. In agreement with [3, 9], they found a very promising site on the Shackleton-de Gerlache Connecting Ridge which they call C1 and which we'll refer to as SdG-C1. Their coordinates

are 222.84E, 89.4505S which we will touch up slightly in our own study by dithering around this site by one 40 m pixels in each direction = 0.13 deg in longitude and 1.3 mdeg in latitude per pixel to clear very local topography.

We inserted a 2.0 m  $\delta$ -function into the DEM at the site under evaluation to represent a solar power mast and applied the horizon elevation [3] method. After dithering, we settled on 222.83E, 89.4398S which is just one pixel away from that in [10], with the results in Fig. 2-1. The subpanels in that Fig. are:

1. The DEM, which is the spatial elevation of a point with reference to the lunar geoid. We will be careful to distinguish between spatial elevation (km) and angular elevation (degrees) where necessary. The x, y coordinates are stereographic.
2. Topocentric angular elevation, which is the angle of a point on the surface as seen from the mast at the site with respect to the local tangent to the geoid and includes the curvature of the geoid.
3. Zoom of item 2, showing some topography at stereographic angle (ccw from x-axis) of 45 degrees.
4. Log-radius polar plot of range to horizon (= location of highest topocentric angular elevation along a stereographic angle). This plot is checked to see if the study is well-sampled (closest obstacle is more than  $\sqrt{2}$  pixels) and complete (the horizon is not beyond the edge of the map).
5. Angular elevation of horizon vs. stereographic angle
6. Angular elevation of horizon vs. local azimuth. This is what we compare to the ephemeris to see if an object is visible.

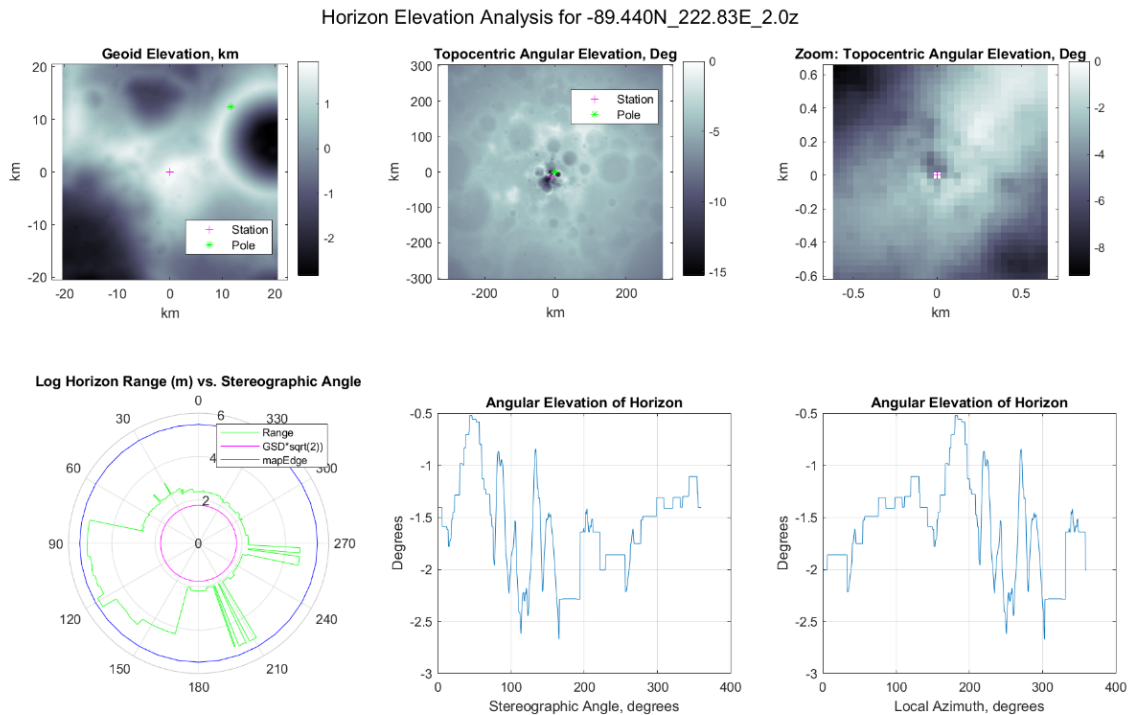


**Fig. 2-1: Horizon Elevation Study of Shackleton - de Gerlache Connecting Ridge C1**

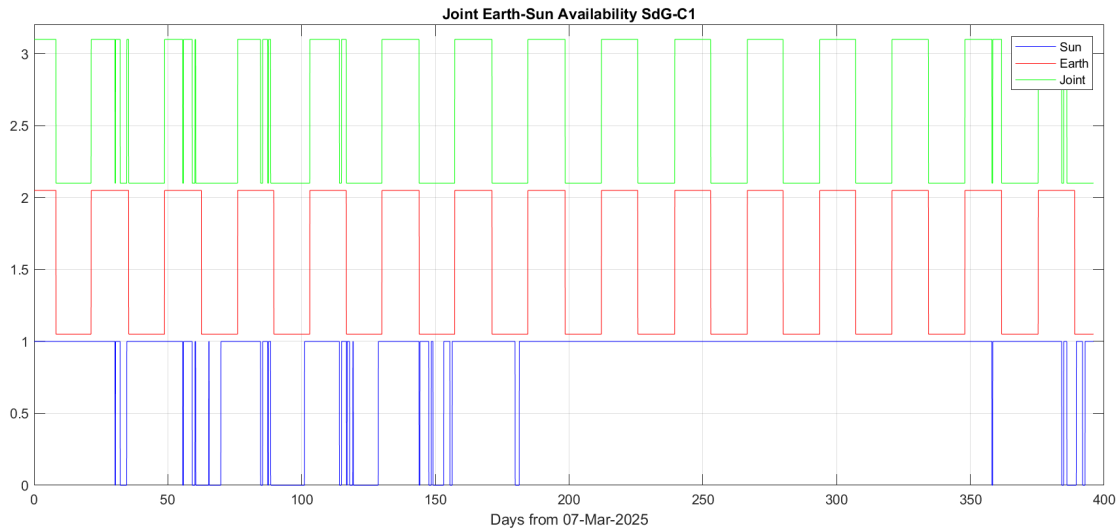


**Fig. 2-2: Sun and Earth Availability at S-dG C1. 1 = available, lines offset for clarity**

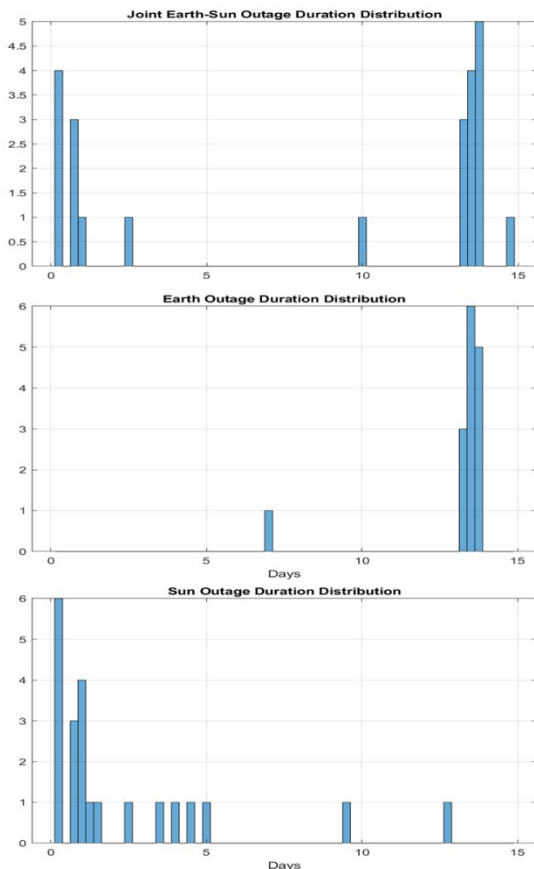


**Fig. 2-3: Outage Histograms for S-dG C1**

Fig. 2-2 shows the Sun and Earth availability timeline for S-dG C1. The Sun is above the topographic horizon for the entire Southern summer, with intermittent outages during the winter. The mean availability is 87% and the longest outage, which occurs in winter, is 12.7 days while most of the rest are of relatively modest duration (Fig. 2-3, bottom panel). The Earth is above the topographic horizon for half of each month, with mean availability is 51% and the longest outage 13.8 days -- compare to 22 h Gateway comm outages or an hour or so LunaNet outages. DWE outages clearly dominate system availability, as shown in Fig. 2-3, so DWE is not a good technical system choice for this location. However, non-technical factors such establishing claims to this valuable territory may be important, in which case an initial operating capability (IOC) first be established with DWE and then the site can be better exploited after a comm relay becomes available.

Another method for calculating solar illumination at lunar sites employs STK, a commercially available software tool, and terrain data from prior lunar missions that may be imported from the NASA PDS (Planetary Data System). This method forms the basis of an ongoing effort to validate the illumination results of the prior sections with an alternative calculational approach utilizing STK's spatial and temporal modeling capabilities. When the STK and horizon elevation methods have been cross-validated, we will use STK for end-to-end mission planning for select lunar surface sites while continuing to use the horizon elevation method to vet sites from the literature, as shown in this paper.

## 2.6 Night Survival

While the longest Sun outages (colloquially referred to as "night") in Fig. 2-3 do not represent a significant difference from the usual 14.5 day nights at lower lunar latitudes, the 14.5 day night survival problem has in some sense already been solved, as shown by the continuing operation of China's Chang'e 4 mission on the lunar Farside after over 33 lunar diurnal cycles [17]. Then, long term survival can be improved by reducing the number of "cold soak" cycles in

which the lowest temperature extremes on the surface must be endured, supporting internal temperatures with radioisotope heating units (RHUs) as used by Chang’e 3 and 4 and various Mars missions, and by buffering the cooling rate after the sun sets. Creative use of heat switches, advanced multi-layer insulation, and thermal capacitor “hockey pucks” can be used towards this end [18].

### 2.7 Site 2: Crater Rim

Inspection of the upper right panel of Fig. 2-1 led to the conjecture “Wouldn’t it be nice if we could find a place on the other side of that local topographic high at 45 degrees stereographic angle which is on the Shackleton rim and would be in the Sun while S-dG C1 is in the shade?” Indeed, such a place was found in [9], which they call site S28 (their Table 4) and we will call SR-S28 after these authors. The longitude is 196.7 and latitude -89.685 (Fig. 2-4). The mean solar availability is 80% -- lower than S-dG C1 – but the longest outage is 6.4 days – half the length of the longest S-dG C1 outage. When both sites are operating jointly, one of them is available 94% of the time and the longest joint outage (when both are offline at the same time) is only 2.7 days. This complementarity is shown in the timeline (Fig. 2-5) and the outage duration histogram (Fig. 2-6).

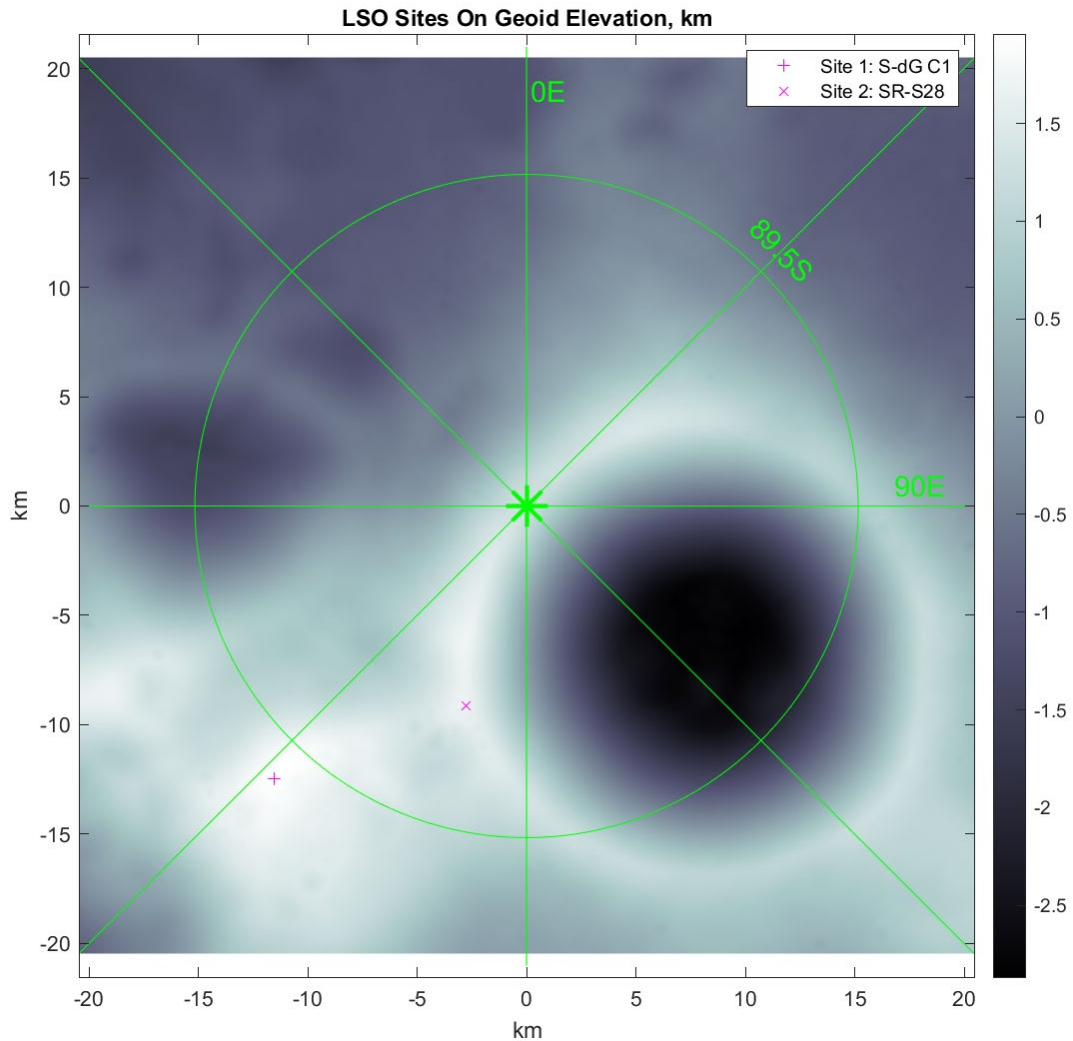


**Fig. 2-4: DEM showing both LSO sites near Shackleton**

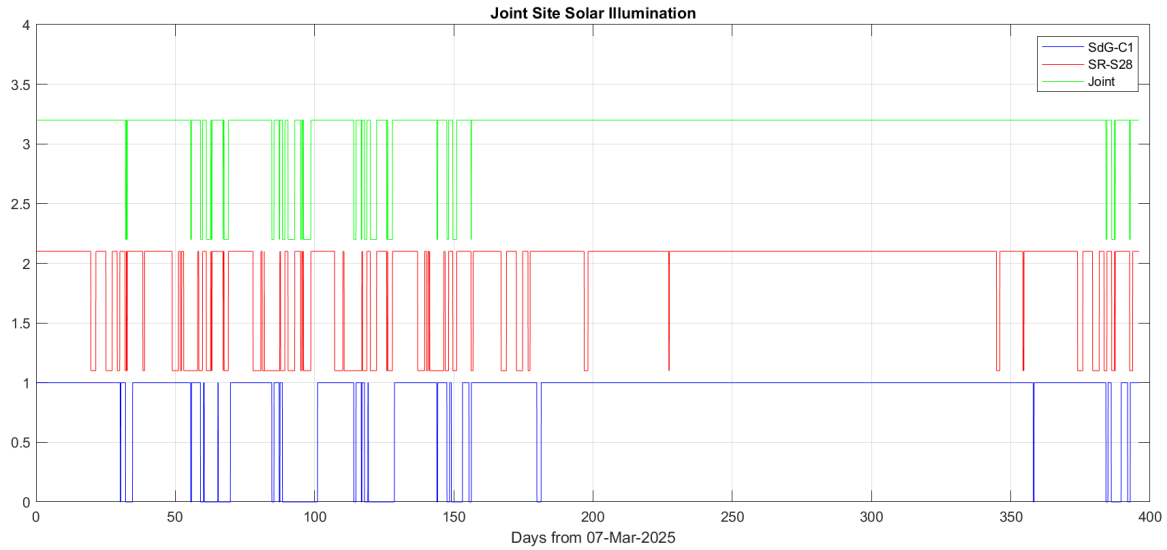


**Fig. 2-5: Joint Solar Operability Timeline for S-dG C1 and SR-S28. 1 = available, lines offset for clarity.**

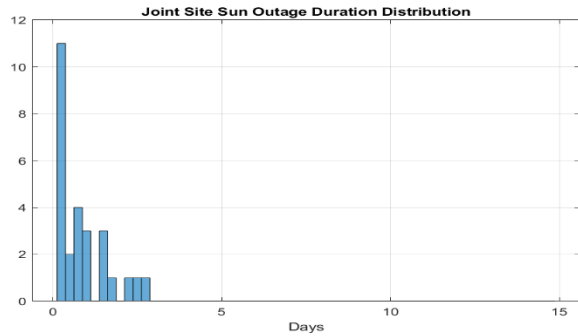


**Fig. 2-6: Joint Sun Outage histogram for S-dG C1 and SR-S28 sites.**

### 2.8 Single-site DWE Optimization

Approximating the topographic horizon for an arbitrary location on the Moon as a uniform -1.5 degrees, after the lower right panel in Fig. 2-1, we find that the highest Sun-Earth joint availability is at zero degree longitude and 84.5S (Fig. 2-7), similar to the VIPER landing site at 54 E, 85 S which was selected for jointly optimal Sun-Earth availability for a limited duration solar DWE mission [19]. Having thus identified the most promising general area of the Moon, we estimate topographic effects by using Earthshine mean intensity from the LPI South Pole Atlas [20] as a rough proxy for DWE availability. Then Earthshine map shows that the region between 10W and 10E longitude and 86S and

85S on the Earth-facing (North) slope of Malapert is promising for long-mission DWE and solar power, in agreement with [21]. More work needs to be done to narrow down the landing site to the right pixel (40 m) for joint solar illumination and DWE.

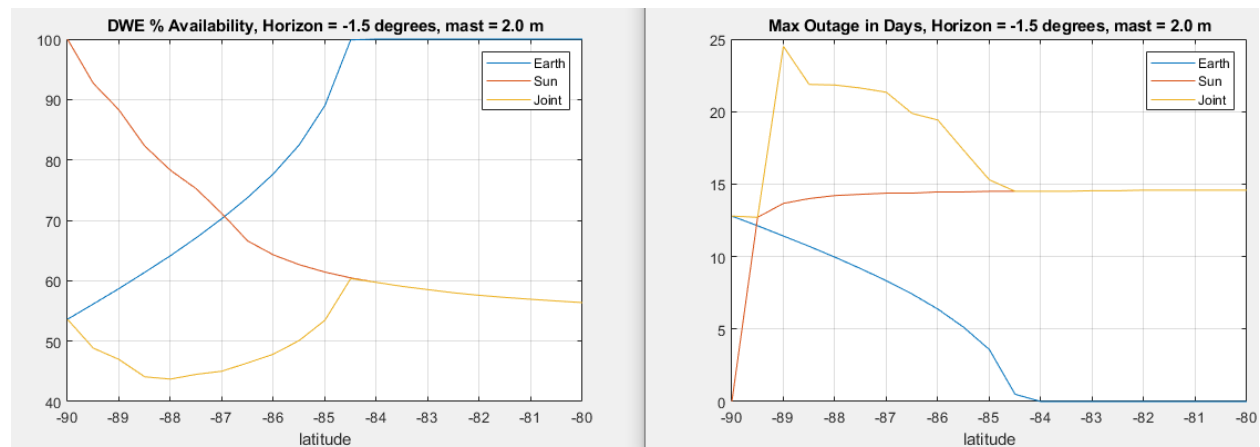


**Fig. 2-7: Joint Availability vs. Latitude for DWE and Solar Power on the Meridian (0E)**

### 3 Local Space Awareness

Local Space Awareness (LSA) means knowing about things that are really close to the sensor and might be overlooked in the design of the primary WFOV payload. For a site on the lunar surface, this means being aware of low-orbit objects (15 - 200 km altitude) which could pass overhead in much less time than it takes the WFOV camera to sweep the sky once (~22 minutes) at the magnitude depth required to accomplish its mission of seeing 1.0 m targets at a range of 6,000 km. Since these close objects are bright, a small pupil but Ultra-Wide FOV camera, or fisheye, can accomplish this mission ([1] §2.5 and 2.6). The key feature of the fisheye camera is that it does not move, staring unblinking at the zenith, so that no orbiting objects can elude it while it is looking in another direction. An existence proof of such a design was shown in last year's paper, which we develop in some depth here.

#### 3.1 Fisheye Design

A fisheye system can be implemented as a single sensor or with smaller FOV sensors; an analysis of mass, volume, focal plane signal chain, and data analysis complexity would be part of that trade. This trade is important since the size and mass of the lens system for each aperture grows rapidly with the single-aperture FOV, as shown below in Fig. 3-1. A 120° full-angle FOV would see objects in the half of the sky > 30° above the horizon, while a 4-camera set of 90° cameras arranged in a quatrefoil would cover almost the entire sky hemisphere. We will develop the 120° full-angle FOV camera optics in some detail since only one optical system and FPA signal chain is required.

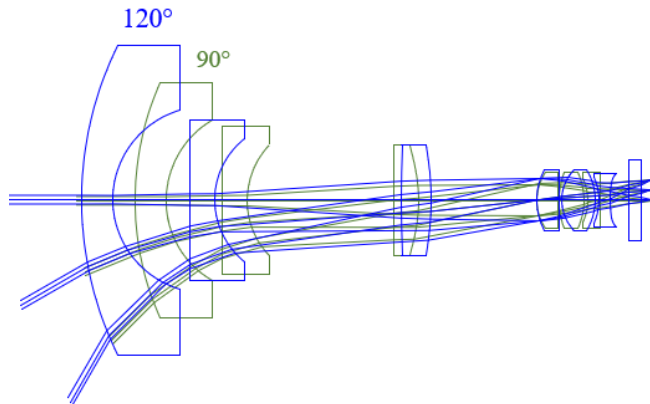


**Fig. 3-1: Comparison of Fisheye Optics Size for 90° and 120° Full-Angle Designs**

performance is achieved with this relatively low lens count in part by including a short wavelength blocking filter on the plano side of either lens 2 or lens 4; the transmission estimate including this “blue blocker” filter is shown in Fig. 3-5.

The 120° optical design, shown by itself in Fig. 3-2, has a maximum lens diameter of ~4.0 inches and is ~7.25 inches from the vertex of L1 to the image. It is comprised of six powered optical elements and delivers an ideal design EE value of  $\geq 0.88$  on 15  $\mu\text{m}$  pixels, providing substantial margin to the 0.25 requirement for fabrication, alignment and thermal degradation for a low cost point telescope, and possibly to trade modest additional cost for higher performance. Fig. 3-3 shows the variation in average entrance pupil diameter (EPD) and IFOV over the field of view. The design exhibits low distortion to the  $F\theta$  mapping function typical of fisheye lenses, Fig. 3-4 shows this mapping function from FPA position to sky angle and the  $\pm 0.4\%$  variation from a simple linear fit of  $R=7.782$  deg/mm. This

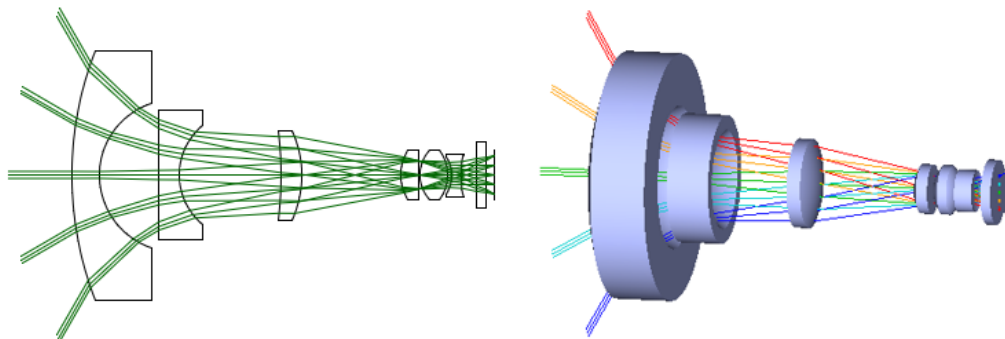


**Fig. 3-2: 120° Fisheye Optical Design**

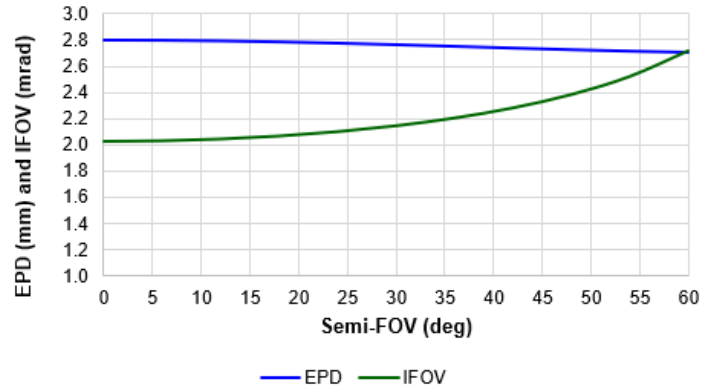


Fig. 3-3: Entrance Pupil Diameter (EPD) and IFOV vs. FOV

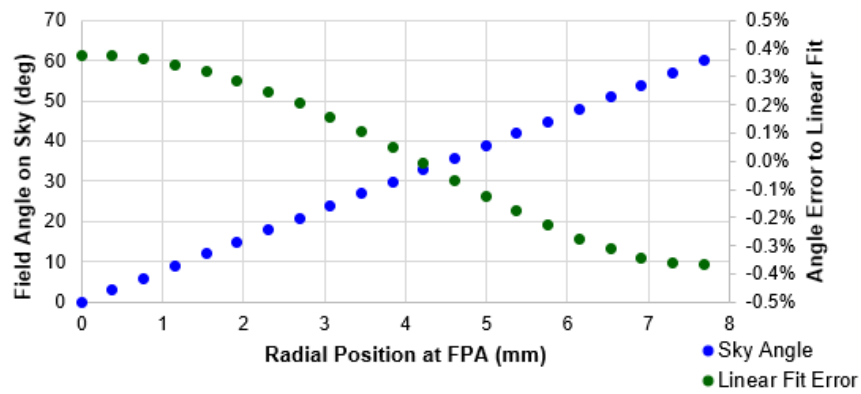


Fig. 3-4: Field Mapping of FPA Radial Position to Sky Angle and Error vs. Linear Fit

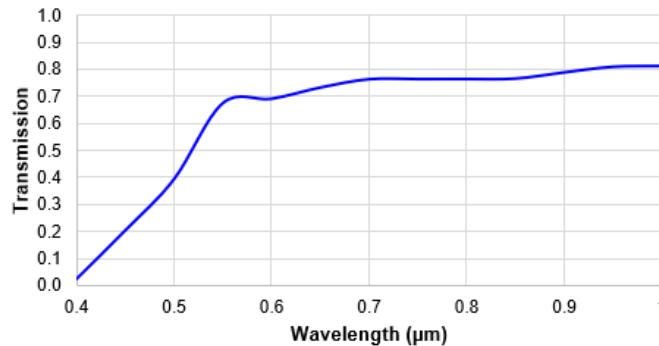


Fig. 3-5: Transmission Estimate with "Blue Blocker" on L2 or L4

### 3.2 Fisheye Radiometry

We take the Caeleste CAE303 "ELFIS2" CMOS focal plane [22], which features

- 1024 x 1024 pixels with 15 μm pitch to fit the optics in §3.1
- TID, SEU, and SEL rad-hard
- Dual Gain, which enables single integration time high dynamic range (HDR) imagery
- 5 e- read noise with a well depth of 160 ke-

And look at the maximum and minimum range targets, with these common parameters

- Integration time = 1.0 s
- Number of frames per data collect = 5. These are averaged in Mission Data Processing (MDP) S/W and the cycle repeats every 5 s.

- Target is a 1.0 diameter, 20% Lambertian albedo target at 90° phase angle.
- The velocity at altitude is for a circular orbit

**Table 3-1: Fisheye Radiometry**

FishEye Radiometry			
Target Range	600	100	15 km
visual magnitude	7.1	3.2	-0.9
Target altitude	300	50	15 km
Target velocity	1.55	1.66	1.67 km/s
Target angular rate	2.59E-03	1.66E-02	1.12E-01 rad/s
Target angular rate	0.15	0.95	6.39 deg/s
Target angular rate	1.26	8.10	54.53 pix/s
Streak length	1.26	8.10	54.53 pix/frame
FOV transit time	810	126	19 s
Target magnitude	7.1	3.2	-0.9
Target signal	204	7,341	326,345 e-
ABP prefactor	0.25	0.25	0.25
ABP factor	0.205	0.058	0.019
VSM target signal	42	427	6070 e-/pix
VSM sky signal	41	41	41 e-/pix
VSM sky noise	6.4	6.4	6.4 e-/pix
VSM total noise	13.7	23.9	78.8 e-/pix
VSM SNR per frame	3.0	17.8	77.0
VSM SNR per collect	6.8	39.8	172.1

We use the single-pixel Visual Sensor Model (VSM) developed by Ball to calculate single-pixel SNR per frame using the Average Best Pixel (ABP). For long streaks (>5 pixels) optimal-aperture extraction may yield better SNR but for conservatism we use the VSM. For combining the 5 frames, we assume that targets with SNR > 3 per frame can be identified and the observations (flux & centroid) averaged rather than the pixels, thus reducing the effective streak length to its single-frame value and allowing  $\sqrt{N_{frames}}$  improvement in SNR. We find that, while objects passing directly overhead have long streaks, they have better SNR because they are much closer, and the fisheye camera can see its bounding case targets, as shown in Table 3-1.

### 3.3 Fisheye Observations of Landings and Launches

As discussed in [5], craft on landing or ascent trajectories will start powered descents coming into the Shackleton region at 15 km altitude about 400 km from the crater. As long as the landing site is not too close to the observing site, the lander will enter the fisheye camera FOV a few minutes before landing as shown in Fig. 3-2. The trajectories in Fig. 3-2 are from [23] One Phase Landing From Orbit (OPLO) with 5 s ticks, corresponding to the fisheye camera collect time. Fig. 3-2 shows the fisheye FOV and two landing trajectories which pass through center of the fisheye FOV:

Vehicle 1 lands 150 km away, while Vehicle 2 lands right next to the LSO site. The fisheye camera will also detect craft flying into and out of the crater following short-hop Vertical Takeoff Vertical Landing trajectories like those shown in [23] which follow higher flight-path angles > 30° for minimum energy or to clear topography.

However, if the landing site is close to the observing site (Vehicle 2), it can elude the 120° fisheye fixed zenith boresight FOV since the terminal flight path angle is 10°. This problem can be addressed by

1. Viewing the lander with the gimbaled WFOV camera if cued by an orbiting sensor that detected the parking to landing orbit maneuver.
2. Revisiting designs for full hemisphere coverage (§3.1 and [1] Fig 2-3).
3. Handing off the terminal landing detection task to proximity sensors, either physical (next section) or EOIR (§4.2).

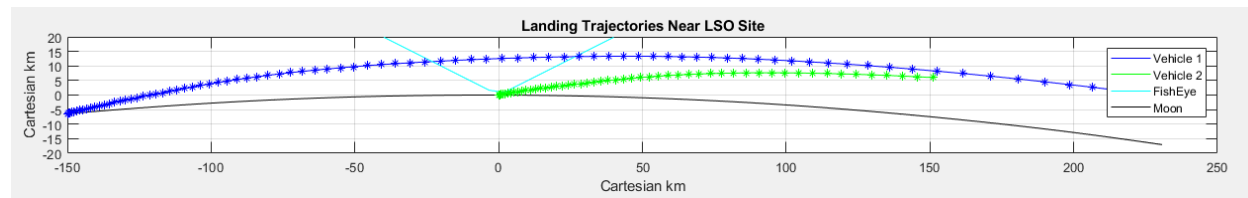


**Fig. 3-2: Landing Trajectories near LSO Site showing the fisheye camera, no vertical exaggeration, 5s ticks**

### 3.4 Dust and Gas Sensors

While we propose the primary SDA phenomenology of the Shackleton LSO is electro-optical it is important to note that other detection methods could be utilized to provide additional lunar activity detection, especially where geometry and lighting conditions make photon (electro-optic and infrared, EOIR) detection difficult or impossible. Such non-photon payloads would provide additional capability for detecting surface mining activities, lunar launches, and landings. This may be considered a form of local space awareness, in the sense that these non-photon particles are in trajectories through space, and are monitoring objects entering or leaving space via the lunar surface. It may also be

considered a form of local lunar surface intelligence, in that the particles have information on activities on the lunar surface itself.

Regolith dust disturbed by landing plumes during a lander's final approach (below 15 km) will spread over thousands of kilometers [26], a much greater range than the photometrically detectable blast zone (BZ) [5, 32]. Sheets of this fine dust will even make it into orbit [26]. Dust will also be stirred up and transported locally by mining and transportation activities on the lunar surface, as may easily be seen in videos of the Apollo moon buggies. To detect this dust, we propose using a temperature-controlled quartz crystal microbalance (TQCM) to detect regolith fallout. The frequency of the quartz crystal decreases as mass lands on the surface of the quartz. If we assume a specific density of the regolith one can determine the amount of regolith dust landing on the surface, with the sensitivity limit on the order of  $2 \times 10^{-9} \text{ g/cm}^2\text{Hz}$  [30] – much less than a monolayer of far-flying ([26] Fig. 3)  $10 - 100 \text{ }\mu\text{m}$  dust particles. The temperature of a dust collection TQCM can be set to ensure no gas is collected on the crystal.

Gas from landings is also detectable locally and even globally.  $\sim 30\%$  of the total exhaust mass is water [29] which increases the exospheric density (primarily non-absorbed water) of the moon [24, 25]. The increased density of the exosphere is greatest in the area surrounding the landing site but migrates globally, in particular to the antipodes of the landing. Within 2 days  $\sim 60\text{-}70\%$  of the water released has been photodestroyed while  $\sim 13\%$  of the exhaust gases have made it to the polar permanently shadowed regions (PSRs) and bound to the regolith by cold traps [25]. This migration of water exhaust gases enables a thermal quartz crystal microbalance (TQCM) anywhere on the surface of the moon to detect the change of exospheric water by monitoring the rate of ice deposition on the crystal surface. To estimate how cold the TQCM would have to be, Fig. 5 of [25] shows the anthropogenic exospheric density an hour after a nearby ( $2^\circ$  or 60 km) landing is about  $1.0$  to  $3.3 \times 10^3 \text{ cm}^{-3}$ . The ideal gas pressure then equals the vapor pressure of water (Fig. 3-3) between 117 and 119 K, so we recommend setting the TCQM temperature to 110 K. To account for collected lunar regolith, as addressed above, the TQCM could be installed facing the lunar surfaces which results in a 100x reduction of dust collection. Alternatively, a single TQCM could be used to both identify dust and water ice collection by heating a sky pointed TQCM periodically which will sublimate the deposited ice. Then one could calculate the condensed ice vs. the collected lunar regolith. The detection limit of  $2 \times 10^{-9} \text{ g/cm}^2\text{Hz}$  [30] is then well less than a monolayer of ice.

Much less work has been done on gas, dust, and photometric signatures of ascent from the lunar surface compared to descent. Partly, this is because to date there have been far fewer return trips from the Moon than landings. Partly, it is because the ascent platform for the largest vehicles has not been the natural lunar surface – for example, the Apollo ascent module blasted off from the descent module. However, the release of gas and its migration is much less dependent on regolith properties than dust excavation, so the gas detection methods discussed here should apply to ascent as well as descent.

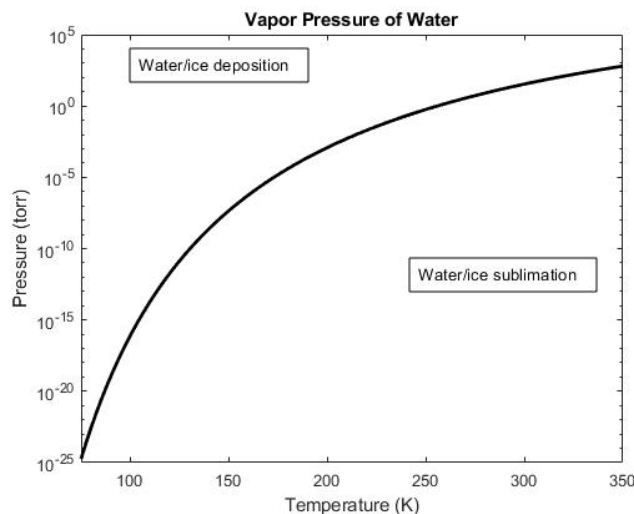


**Fig. 3-3: Vapor pressure of water, for exhaust gas sensing**

## 4 Local Lunar Surface Intelligence

While awareness of near-lunar *space* is the minimum mission of the LSO, an enhanced *surface* observation payload suite would perform multiple missions: awareness of human activities on the surface, characterization of the Moon for exploration, and basic scientific knowledge. Note that sensing of gas and dust is a gray area which may be considered observations of both space and the disturbed lunar surface and is discussed in the previous chapter.

### 4.1 Viewing the Shackleton PSR

All of the crater interior is visible from Site 2 as shown in Fig. 4-1. This figure is an intermediate product of the horizon elevation analysis and includes the curvature of the lunar geoid for a 3D Cartesian representation of the surface and lines of sight.

Approximating Shackleton as a spherical crater with a width-to-depth ratio of 10, we apply the model from [5, 11] to show that the VIS light levels at summer solstice are about 1/7,000 that of direct sun on a rock normal to both the sun and the camera. Hence a VIS ground-viewing camera in the enhanced instrument suite must have a dynamic range  $> 7,000$  and be able to integrate for a few seconds to develop an image. An example is the HDR camera on the recently selected VISE instrument suite to be built by Ball for delivery to the lunar surface. Of course, the crater interior is *really* dark and cold at winter solstice, though even then equipment mining the PSR should stand out brightly in a thermal-IR bolometer camera such as the L-CIRiS built by Ball for delivery to the lunar surface and described below.

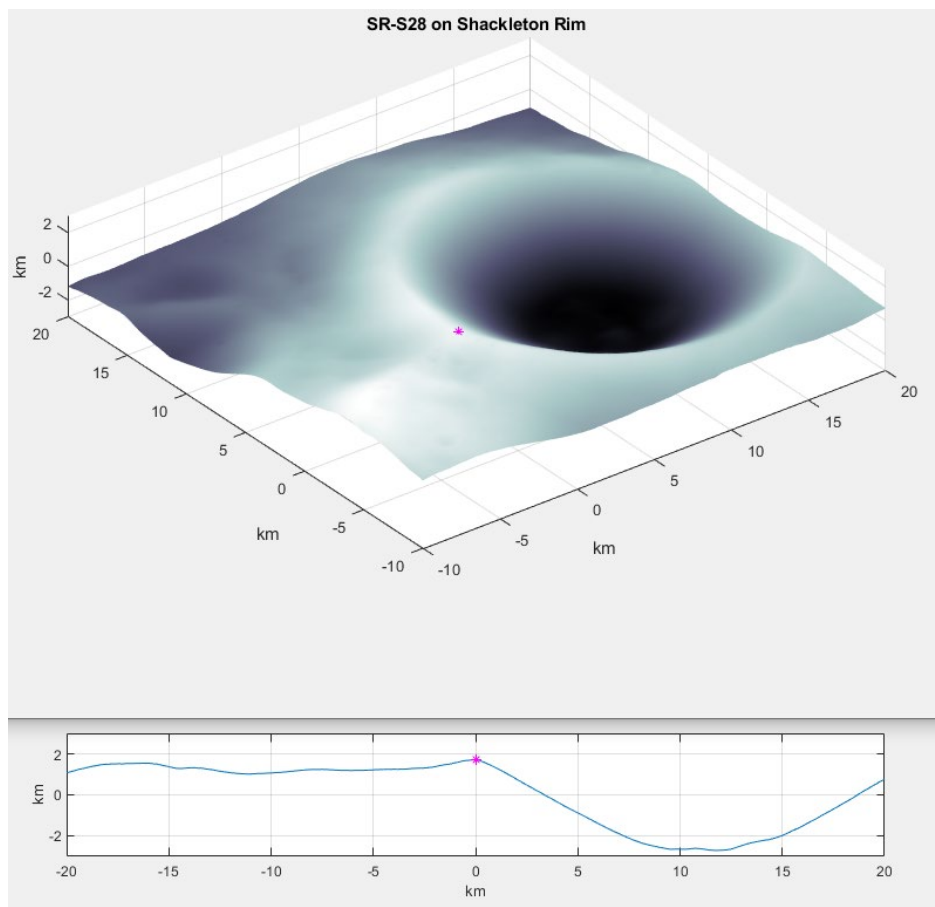


**Fig. 4-1: Site 2 (SR-S28) can see into Shackleton. Top: oblique 3d Cartesian view of curvature-corrected DEM, no vertical exaggeration. Bottom: slice through Site 2.**

### 4.2 Sensor Suite Example: VISE

An example of a science instrument suite for the lunar surface is Lunar-VISE (Lunar Vulkan Imaging and Spectroscopy Explorer), a payload selected by NASA through the PRISM (Payloads and Research Investigations on the Surface of the Moon) program for development by Ball Aerospace. Although the landing site is the Gruithuisen

domes region, Lunar-VISE's geological and thermophysical measurement capabilities are broadly applicable to lunar surface observation, including regions adjacent to the LSO sites. A NASA CLPS (Commercial Lunar Payload Services) lander is scheduled to transport Lunar-VISE in late 2026 to Gruithuisen where two suite instruments will operate from the lander and three from a rover. All Lunar-VISE instruments possess design heritage to prior flight payloads.

The LV-VIMS (Lunar-VISE Visible/Infrared Multiband Suite) is a rover-mounted unit combining two co-boresighted radiometric imaging instruments on a common rotation stage. Rotations of the turntable platform scan the FOVs of the multispectral visible instrument (seven bands from 350 to 960 nm) and thermal infrared instrument (four bands from 7.2 to 14.0  $\mu\text{m}$ ), generating panoramic images up to 180° wide in azimuth (Fig. A). Owing to an intermediate optical focus, individual images may include features at a range from < 4m out to the distant horizon, with high image quality throughout (Fig. B). A foreground spatial resolution < 1 cm is well suited to the study of small scale phenomena such as regolith structure and micro-cold traps [33] while the same IFOV at km range could characterize vehicles and surface disturbances at ~ 0.5 m GSD. Of particular interest at Shackleton and other craters may be the LV-VIMS infrared radiometer capability for remote temperature imaging of persistent and intermittent shadowed regions within craters, and heat-emitting equipment in those regions. In this mode, the radiometer could also reveal regions likely to retain water ice, and to investigate trafficability by means of thermophysical studies of subsurface structure.

The LV-VIMS takes its basic design from Ball's L-CIRiS (Lunar-Compact Infrared Radiometer in Space), multispectral thermal infrared imaging radiometer (Fig. A). The updated unit expands the L-CIRiS chassis to accommodate the additional visible radiometric camera sharing the common rotation stage. Thermal infrared bands include one broad band (9 to 14  $\mu\text{m}$ ) for remote temperature imaging, and three for mineral identification by spectral emission. The seven visible bands enable spectral reflectivity measurements for several purposes including composition and regolith maturity. Entirely uncooled operation contributes to high reliability, longer lifetime and low size, weight and power.

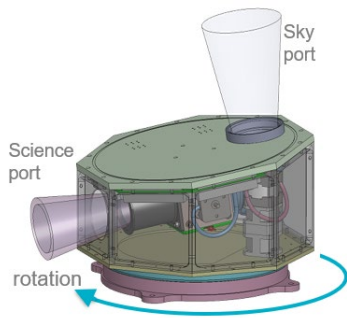


**Fig. A.** The LV- VIMS instrument updates the L- CIRiS thermal infrared imaging radiometer (shown above) by adding a visible imaging radiometer on the same rotation stage



**Fig B.** LV-VIMS produces panoramic images in 11 visible and IR bands, like the simulation in two bands, above.

**Fig. 4-2: Instrumentation to Characterize the Surface near Observatory Sites**

The Lunar-VISE GRNS (Gamma Ray and Neutron Spectrometer) records the spectra of gamma rays and neutrons emanating from beneath the lunar surface, providing data on elemental composition and abundance. An energy detection range from < 0.3 eV to 10 MeV spans gamma ray line energies, and neutron continuum energies generated by key lunar geological elements including Th, U, K, Fe, Si, and Mg. Detection extends to depths up to ~1 m and over a ~1 m diameter. At Gruithuisen domes, the time to collect sufficient elemental abundance data to fulfill Lunar-VISE science objectives is 15 minutes for gamma ray spectra and 4 hours for neutrons. The LV-GRNS is a rebuild, with minor modifications, of the Miniature Neutron Spectrometer recently delivered for the upcoming LunaH-Map mission [27]. A similar instrument may be of interest in detecting sources of nuclear energy on the lunar surface. For example, [28] developed drone-portable gamma and neutron mapping instrumentation which detected and localized surrogate Special Nuclear Materials in real-time; such lightweight instrumentation would be well-suited to the lunar surface.

Two Lunar-VISE visible HDR cameras are mounted on the lander for characterizing the landing zone and rover traverse. The nadir-facing descent camera views the surface before, during and after scouring by the lander plume, providing data on regolith geotechnical properties, dust lofting and other phenomena. The side-mounted context camera takes >270° panoramic images of the landing site, for use in planning the initial rover traverse in the Lunar-VISE science mission. Such cameras could be used at Shackleton Station sites for observing landing/takeoff activity beneath the fisheye FOV (§3.3) and observe activity in the sunlight areas in the vicinity of the crater and in the PSR during lunar summer.

#### 4.3 Accommodating Lunar instruments on Commercial Landers

L-CIRiS and VISE are taking advantage of the availability of commercial services, facilities, and space vehicles for lunar missions in order to reduce costs by up to 4x over traditional missions transporting payloads to the Moon. For perspective, the cost of the 1960's Surveyor project was \$4.3 B in 2022 \$ for 5 successful missions [31], while CLPS missions are on the order of \$100 M each with a notional 50% success rate. However, this partnership requires some system and interface choices that would formerly have been imposed by a space agency and instead must developed through direct engagement between the payload and commercial lander developers. Representative examples which arose during our development of L-CIRiS and VISE, which would apply to all the instrumentation delivered for Shackleton Station, include the following:

- Storage location for science data – how much, if any, is in the instrument, how much in the lander, or is it divided between the two?
- Payload and lander CONOPS may each impose constraints on when data can be transferred. Can all constraints be fulfilled?
- Instrument operation may require command sequences. Will these be sequences or scripts resident in instrument software or firmware, or can the lander store them? The answer to the latter question may determine if command sequences can be modified from the ground.
- There may be periods when lander power is absent, for example during landing. Can the payload stay safe during these times?
- Lander orientation on the lunar surface impacts payload illumination conditions, and therefore the thermal environment. Can the orientation be controlled sufficiently, or must payload thermal design accommodate a range of thermal conditions?

The list of similar issues is long.

## 5 Conclusions

The development of scientific and commercial capabilities for the surface of the Moon in the 2023-2030 time frame opens the door to observing stations on the surface of the Moon which can watch over near-lunar space and objects entering and leaving that space via the lunar surface. These observations can take the form of photons, both visible and thermal IR, as well physical particles such as gas molecules and dust plumes from rocket exhaust.

## 6 References

- [1] J. E. Van Cleve, A. M. Lawitzke, E. MacAnlis, et al., Hiding in plain sight: observing objects in low lunar orbit and the L2 dark cone from a lunar surface observatory, *AMOS 2021*
- [2] P. Zimmer J. T. McGraw, and M. R. Ackermann, Cislunar SSA/SDA from the Lunar Surface: COTS Imagers on Commercial Landers, *AMOS 2021*
- [3] E. Mazarico, G. A. Neumann, D. E. Smith et al, Illumination conditions of the lunar polar regions using LOLA topography, *Icarus*, 211:1066-1081, 2011
- [4] A. M. Lawitzke, J. Van Cleve, J. Contreras et al., Hybrid Sensor for Joint Space Domain Awareness and Lunar Surface Intelligence, *AMOS 2022*
- [5] D. P. Osterman, J. Van Cleve, A. M. Lawitzke et al., Anthropogenic Change Detection On and Close to the Moon for Space Domain Awareness, *AMOS 2022*
- [6] H. M. Brown, A. K. Boyd, B. W. Denevi et al., Resource potential of lunar permanently shadowed regions, *Icarus*, 377:114874, 2022
- [7] C. Chow, J. Wetterer, K. Hill et al, Cislunar Periodic Orbit Families and Expected Observational Features, *AMOS 2020*
- [8] P. Dao, K. Haynes, V. Frey et al., Simulated Photometry of Objects in Cislunar Orbits, *AMOS 2020*

- [9] E. J. Speyerer and M. S. Robinson, Persistently illuminated regions at the lunar poles: Ideal sites for future exploration, *Icarus*, 222:122-136, 2013
- [10] P. Glaser, J. Oberst, G. A. Neumann et al., Illumination conditions at the lunar poles: Implications for future exploration, *Planetary and Space Science*, 162:170-178, 2018
- [11] A. P. Ingersoll, T. Svitek, and B. C. Murray, Stability of Polar Frosts in Spherical Bowl-Shaped Craters on the Moon, Mercury, and Mars, *Icarus*, 100:40-47, 1992
- [12] E. Mazarico, M. K. Barker, and J. B. Nicholas, Advanced illumination modeling for data analysis and calibration. Application to the Moon, *Space Research*, 62:3214-3228, 2018
- [13] J. Foust, *Space News*, <https://spacenews.com/draeper-wins-nasa-contract-for-farside-lunar-lander-mission>, 2022
- [14] A. Jones, *Space News*, <https://spacenews.com/china-to-build-a-lunar-communications-and-navigation-constellation>, 2022
- [15] R. Whitley and R. Martinez. Options for Staging Orbits in Cis-Lunar Space. *2016 IEEE Aerospace Conference*, 2016.
- [16] E. M. Zimovan Spreen, Trajectory Design and Targeting for Applications to the Exploration Program in Cis-lunar Space, PhD Dissertation, Purdue U., 2021
- [17] A. Jones, *Space News*, <https://www.space.com/china-chang-e-4-moon-far-side-1000-days>, 2021
- [18] J. E. Van Cleve, J. D. Weirner, C. R. Neal et al., Darkness Visible: Instrumentation and Thermal Design to Access the Hidden Moon, *Survive the Lunar Night* Poster <https://www.hou.usra.edu/meetings/survivethenight2018/eposter/7005.pdf>, 2018
- [19] J. Foust, *Space News*, <https://spacenews.com/nasa-picks-landing-site-for-viper-lunar-rover>, 2021
- [20] J. Stopar, Lunar South Pole Radar Images and Earthshine Mode (85°S to Pole), Lunar and Planetary Institute Regional Planetary Image Facility, LPI Contribution 2347, <https://repository.hou.usra.edu/handle/20.500.11753/1488>
- [21] N. E. Petro and D. P. Moriarty III, Mons Malapert: A Site in Support of Exploration of the Lunar South Pole and Earth Observations, *Lunar Surface Science Workshop 2012 (LPI #2241)*, paper 8015, 2021
- [22] <https://caeleste.be/wp-content/uploads/2021/03/ELFIS2-Leaflet.pdf>
- [23] H. Chu, L. Ma, K. Wang et al., Trajectory optimization for lunar soft landing with complex constraints, *Advances in Space Research*, 60:2060-2076, 2017
- [24] W. M. Farrell, P. Prem, O. J. Tucker et al., A lingering local exosphere created by a gas plume of a lunar lander, *Icarus*, 376:114857
- [25] P. Prem, D. M. Hurlley, D. B. Goldstein, and P. L. Varghese, The Evolution of a Spacecraft-Generated Lunar Exosphere, *JGR Planets*, 125 <https://doi.org/10.1029/2020JE006464>, 2020
- [26] P. T. Metzger, Dust Transport and Its Effects Due to Landing Spacecraft, *Lunar Dust Conference LPI No. 2141*, paper 5040
- [27] E. B. Johnson, C. Hardgrove, R. Starr et al., Development of the LunaH-Map miniature neutron spectrometer, *Proc. SPIE 10392, Hard X-Ray, Gamma-Ray, and Neutron Detector Physics XIX*, 103920H, 2017
- [28] R. Pavlovsky, J. W. Cates, W. J. Vanderlip et al., 3D Gamma-ray and Neutron Mapping in Real-Time with the Localization and Mapping Platform from Unmanned Aerial Systems and Man-Portable Configurations, arXiv:1908.06114, 2019
- [29] K. H. Lee, Numerical comparison of exhaust plume flow behaviors of small monopropellant and bipropellant thrusters. *PLoS ONE*, 12(5), e0176423. <https://doi.org/10.1371/journal.pone.0176423>, 2017
- [30] <https://crystaltekcorp.com/products/tqcm>
- [31] [https://en.wikipedia.org/wiki/Surveyor\\_program](https://en.wikipedia.org/wiki/Surveyor_program)
- [32] R. N. Clegg, B. L. Joliff, M. S. Robinson et al., Effects of rocket exhaust on lunar soil reflectance properties, *Icarus*, 227:176-194, 2014
- [33] P. O. Hayne, O. Aharonson, and N. Schorghofer et al., Micro Cold Traps on the Moon, *Nature Astronomy*, 5:169-175, 2021